GENETICS

Global chromatin relabeling accompanies spatial inversion of chromatin in rod photoreceptors

Cheryl L. Smith[1], Yemin Lan[1], Rajan Jain[1,2], Jonathan A. Epstein[1,2]*, Andrey Poleshko[1]*

The nuclear architecture of rod photoreceptor cells in nocturnal mammals is unlike that of other animal cells. Murine rod cells have an "inverted" chromatin organization with euchromatin at the nuclear periphery and heterochromatin packed in the center of the nucleus. In conventional nuclear architecture, euchromatin is mostly in the interior, and heterochromatin is largely at the nuclear periphery. We demonstrate that inverted nuclear architecture is achieved through global relabeling of the rod cell epigenome. During rod cell maturation, H3K9me2-labeled nuclear peripheral heterochromatin is relabeled with H3K9me3 and repositioned to the nuclear center, while transcriptionally active euchromatin is labeled with H3K9me2 and positioned at the nuclear periphery. Global chromatin relabeling is correlated with spatial rearrangement, suggesting a critical role for histone modifications, specifically H3K9 methylation, in nuclear architecture. These results reveal a dramatic example of genome-wide epigenetic relabeling of chromatin that accompanies altered nuclear architecture in a postnatal, postmitotic cell.

INTRODUCTION

In eukaryotic cells, DNA is packaged into chromatin and organized in subnuclear compartments (1–3). This compartmentalization effectively separates transcriptionally active and inactive chromatin in three-dimensional (3D) space, promotes efficient regulation of gene expression, and maintains heterochromatin silencing [reviewed in (4–7)]. Typically, the epigenetically silenced, condensed heterochromatin is positioned at the nuclear lamina and around nucleoli, while transcriptionally active and less condensed euchromatin is found in the nuclear interior. Such nuclear organization is referred to as conventional nuclear organization and has been observed in all but one eukaryotic cell type: the rod photoreceptor cell of nocturnal mammals (8).

The 3D organization of chromatin contributes to physical properties of the nucleus such as mechanical force response, cell migration, signaling, and transparency to light (9). Evolution has selected for some of these nongenetic functions. For example, the rod photoreceptor in nocturnal animals is a light-sensitive neuron that has adapted its chromatin organization to enhance light sensitivity (10). In these rod cells, heterochromatin is condensed in the center of the nucleus, while euchromatin is located at the nuclear periphery. This fundamental reorganization of the spatial positioning of chromatin produces nuclei with so-called "inverted" nuclear architecture (8).

Retinal tissue is composed of multiple cell types including bipolar cells, ganglion cells, horizontal cells, amacrine cells, and rod and cone photoreceptor cells. These cells all originate from the same precursor cells, which exhibit conventional nuclear architecture (8, 11, 12). In contrast to cone photoreceptors, rod cells of nocturnal animals form the inverted chromatin spatial pattern by remodeling the conventional nuclear organization during maturation. This inverted nuclear organization has been observed in rod cells of many nocturnal and aquatic mammals including rodents, cats, dogs, and dolphins (10).

Several studies have described chromatin inversion in rod photoreceptors (10, 13–16). In mice, chromatin inversion occurs during the first few weeks of postnatal life when committed rod cells also exit the cell cycle and become post mitotic (8). During this time, heterochromatin from the nuclear periphery is relocated to the nuclear interior and forms a dense structure in the center of the nucleus. Previous studies have shown that mature rod cells lack two proteins, Lamin B receptor (LBR) and Lamin A/C, that normally tether heterochromatin to the nuclear periphery (10). While Lamin A/C expression is also absent in retinal progenitor cells (RPCs) (15), LBR is lost midway through rod cell maturation. Knockdown of both LBR and Lamin A/C results in repositioning of histone H3 Lys9 trimethyl (H3K9me3)– and H4K20me3-marked heterochromatin from the nuclear periphery (10, 17). However, cells with LBR and Lamin A/C knockout or knockdown do not fully mimic the chromatin inversion observed in rod cells. Lack of LBR and Lamin A/C results in release of heterochromatin from the nuclear periphery, but heterochromatin fails to form a single mass in the center of the nucleus, and euchromatin repositioning to the nuclear periphery is incomplete (10). This suggests that spatial reorganization of chromatin in rod cells is dependent upon additional mechanisms.

Here, we demonstrate that the spatial chromatin reorganization that occurs in maturing rod photoreceptors is accompanied by global epigenetic changes of histone H3 Lys9 methylation. During this process, lamina-associated domains (LADs), which form nuclear peripheral heterochromatin and are marked with histone H3 Lys9 dimethyl (H3K9me2) in immature rod cells, are relabeled with H3K9me3 concomitant with repositioning from the nuclear periphery to the nuclear interior. In contrast, euchromatin regions, which are enriched for active chromatin marks and found in the nuclear interior before rod cell maturation, accumulate H3K9me2 histone modification and reposition to the nuclear periphery. We observe these global changes in H3 Lys9 methylation occurring after rod cells have exited the cell cycle and in parallel with spatial reorganization of chromatin. Our data indicate that chromatin inversion is achieved through epigenome reprograming and suggest a role for histone modification in the spatial organization of the genome.

[1]Department of Cell and Developmental Biology, Penn Epigenetics Institute, Perelman School of Medicine, University of Pennsylvania, Philadelphia, PA, USA. [2]Department of Medicine, Penn Cardiovascular Institute, and Institute of Regenerative Medicine, Perelman School of Medicine, University of Pennsylvania, Philadelphia, PA, USA.
*Corresponding author. Email: poleshko@pennmedicine.upenn.edu (A.P.); epsteinj@pennmedicine.upenn.edu (J.A.E.)

RESULTS

H3K9me2 marks chromatin at the nuclear periphery in cells with conventional and inverted nuclear organization

The mammalian retina is composed of many neuronal cell types including cone and rod photoreceptor neurons. Both types of photoreceptors originate from RPCs during embryonic development (*11*). Later, during postnatal development, rod cells adopt a unique, inverted chromatin organization, which differs from other cell types, including the RPCs from which they are derived (Fig. 1A). In a conventionally organized nucleus, heterochromatin can be visualized as dense DAPI (4′,6-diamidino-2-phenylindole)–stained regions often marked with repressive histone modifications, such as H3K9me3, and is observed at the nuclear periphery and within chromocenters.

Conversely, less condensed euchromatin is marked with active histone modifications, like H3K9ac, and is found in the nucleoplasm (Fig. 1B). In contrast to this conventional pattern, DAPI staining of inverted nuclei in mouse rod cells shows heterochromatin packed in the center of the nucleus and euchromatin at the nuclear periphery (Fig. 1B). Consistent with this spatial reversal of heterochromatin and euchromatin, we observed that several repressive and active histone modifications are also inverted in rod cell nuclei (Figs. 1B and fig. S1). H3K9me2 has been shown to mark the heterochromatin of LADs at the nuclear periphery in cells with conventional nuclear architecture (*18*, *19*). However, we found that H3K9me2-modified chromatin remains at the nuclear periphery in rod cells with inverted nuclei (Fig. 1C). LADs, as part of heterochromatin, are expected to
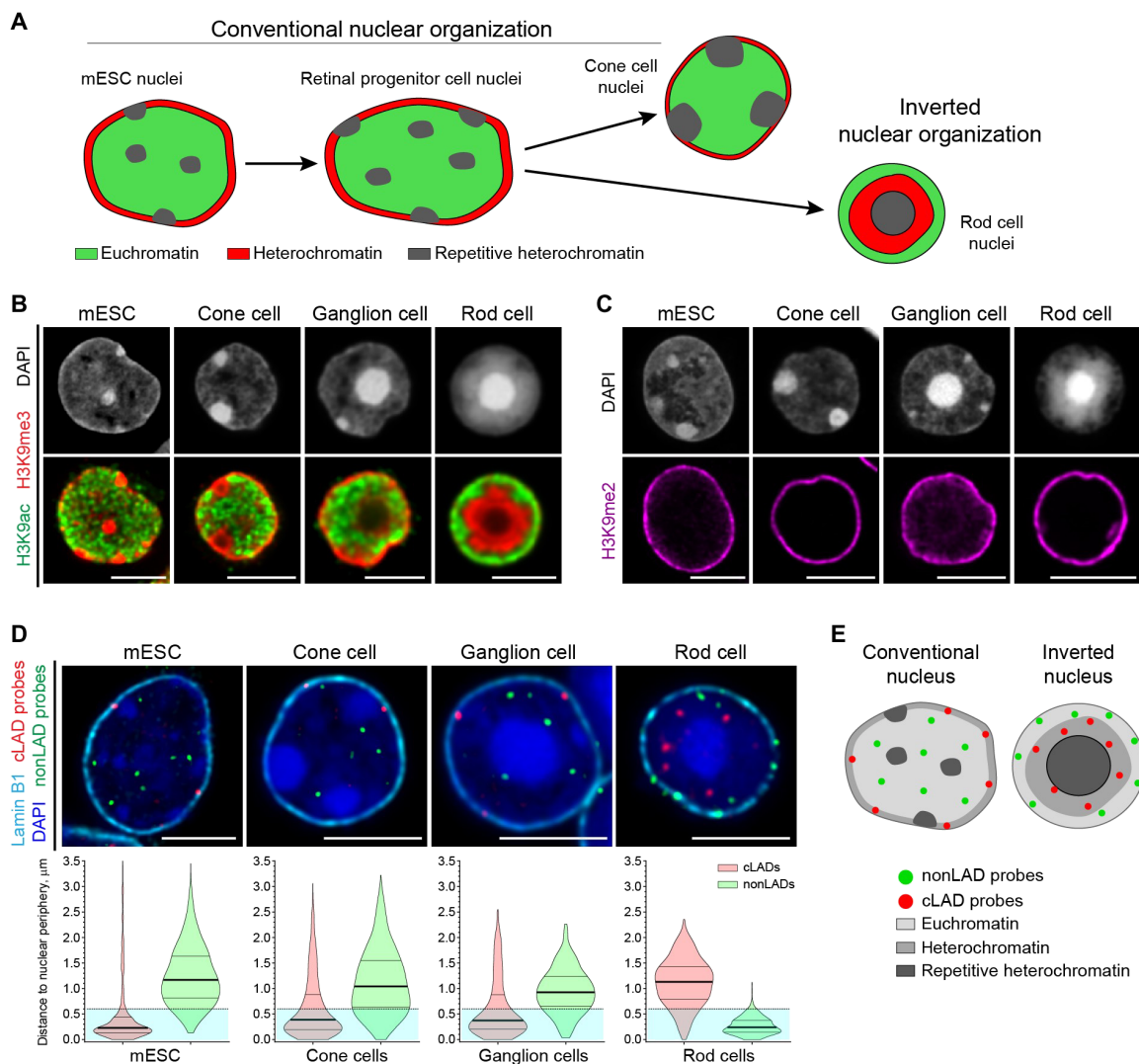

Fig. 1. H3K9me2 marks chromatin at the nuclear periphery in cells with conventional and inverted nuclear organization. (**A**) A schematic representation of retinal cell differentiation and spatial chromatin inversion in murine rod photoreceptors. (**B** and **C**) Representative immunofluorescent confocal images of a mouse embryonic stem cell (mESC) and retinal cells stained for 4′,6-diamidino-2-phenylindole (DAPI) and indicated histone modifications. (**D**) Representative confocal images (top) of indicated cell types hybridized with fluorescent DNA oligoFISH probes targeting genomic regions in cLADs (red) and nonLADs (green), immunostained for Lamin B1 (cyan), and counterstained with DAPI (blue). Violin plots (bottom) show distribution of distances to the nuclear periphery (as defined by Lamin B) of individual cLAD (red) and nonLAD (green) probes. *n* = 25 cells, minimum 600 loci. Dotted lines indicate average thickness of H3K9me2 peripheral chromatin layer and the peripheral zone is highlighted (light blue). (**E**) A schematic illustration of localization of heterochromatin cLADs (red, medium gray) and euchromatin nonLADs (green, light gray) in conventional and inverted nuclei. Lines on violin plots show median, 25th and 75th percentiles. Scale bars, 5 μm.

relocate to the center of the nuclei of rod cells. If that is the case, then LADs that relocate to the nuclear interior during rod cell maturation must lose H3K9me2.

To test the localization of LAD regions in inverted and conventional retinal cells, we used a library of oligo probes targeting constant LAD (cLAD) and constant inter-LAD (nonLAD) regions (20). cLAD and nonLAD genomic regions were previously defined as regions that are constant in their assigned category across multiple cell types including mouse embryonic stem cells (mESCs), fibroblasts, and neuronal cells (21). As expected, in conventionally organized mESCs, cone cells, and ganglion cells, we observed cLADs at the nuclear periphery and nonLADs in the nuclear interior (Fig. 1, D and E). In contrast, cLADs in rod cells were found in the nuclear interior, confirming their repositioning (Fig. 1, D and E), and nonLADs were at the nuclear periphery (Fig. 1, D and E). Like rod cells, ganglion cells have a noticeable clustering of central heterochromatin (Fig. 1, B to D), but they do not have an inverted chromatin architecture: cLADs remain at the nuclear periphery, and nonLADs remain in the nucleoplasm (Fig. 1D).

Spatial chromatin inversion is accompanied by global changes of histone H3 Lys9 methylation

To determine whether chromatin in rod photoreceptors has undergone global epigenetic changes, we assayed genome-wide distributions of H3K9me2, H3K9me3, and H3K9ac histone modifications in rod cells from adult mice for comparison with the same marks in mESCs (Fig. 2A). Rod cells were sorted by flow cytometry from dissociated whole retinal tissue of adult animals (fig. S2; see Methods), and each histone modification was assessed using cleavage under targets and release using nuclease (CUT&RUN) (22). We compared these genome-wide histone modification data with existing datasets describing cLADs and nonLADs (19, 21) and with H3K9me2, H3K9me3, and Lamin B CUT&RUN data from mESCs (Fig. 2A; this study). As has been observed previously, cLADs in mESCs are enriched for H3K9me2 and, to a lesser extent, also for H3K9me3, while nonLADs are depleted for both of these marks (18, 19, 23, 24). In comparison to the same regions in mESCs, we observe a marked reduction of H3K9me2 in cLAD regions in rod cells as well as a marked increase in H3K9me3 in those domains (Fig. 2, A to C). nonLADs in rod cells show some increase in H3K9me2 over nonLADs in mESCs (Fig. 2, A to C). cLADs and nonLADs together account for more than 70% of the genome (21). We compared H3K9me2 and H3K9me3 in mESCs and adult rod cells and found that the H3K9 methylation status changes in more than 75% of the genome (fig. S3, A and B). Thus, rod cells have undergone global epigenetic relabeling. In terms of overall genome coverage, both H3K9me2 and H3K9me3 label approximately the same percentages in mESCs and adult rod cells (fig. S3B).

Examination of H3K9 methylation status in cLADs revealed that H3K9me3 labels 89% of cLAD base pairs in adult rod cells (Fig. 2B). Consistent with this observation, the distribution of normalized H3K9me3 signal in all cLAD regions increases markedly from mESCs to adult rod cells, while the H3K9me2 distribution shows a notable reduction (Fig. 2C and fig. S3C). Relabeling of H3K9 is also observed in nonLAD regions, but in nonLADs, H3K9me2 increases and H3K9me3 is reduced (Fig. 2C and fig. S3C). Overall, we observed that 42% of nonLAD base pairs showed an increase in H3K9me2 in rod cells as compared to mESCs (Fig. 2B).

We also assessed cLADs and nonLADs for enrichment of H3K9me2- and H3K9me3-modified chromatin using a statistical analysis for enrichment (see Methods) and found that, in mESCs, cLADs were enriched for H3K9me2 (1.62-fold observed over expected by chance, performed with 1000 permutations per test) and for H3K9me3 (1.77-fold). In contrast, cLADs in rod cells were depleted for H3K9me2 (0.75-fold observed over expected) but still enriched for H3K9me3 (1.95-fold) (all P values <1.00×10^{-3}; Fig. 2D; see Methods and table S2). In both mESCs and rod cells, nonLADs were depleted for H3K9me3 (0.25- and 0.11-fold, respectively). nonLADs were also depleted for H3K9me2, although much more so in mESCs (0.22-fold observed over expected) than in adult rod cells (0.84-fold) (Fig. 2D). Together, our results demonstrate that H3K9me2, a mark of peripheral chromatin that is enriched in cLADs in mESCs, is depleted in cLADs of adult rod cells (Fig. 2D). In comparison, H3K9me3, which is fairly equally distributed across the genome of cells with conventional nuclear organization, was highly enriched only in cLADs and significantly depleted in nonLADs of adult rod cells (Fig. 2D). This is consistent with colocalization of cLAD oligonucleotide fluorescence in situ hybridization (oligoFISH) probes and H3K9me3-marked chromatin in the nuclear interior of adult rod cells (Figs. 1, B and D). Euchromatic nonLADs in rod cells colocalize with acetyl-H3 and H3K9me2 histone modifications at the nuclear periphery (Fig. 1 and fig. S1).

We assessed the redistribution of H3K9me2 not only in cLADs but also in other functional genomic elements in adult rod cells compared to mESCs. In long interspersed nuclear elements (LINEs), which have previously been shown to be abundant in LADs (21), H3K9me2 shifts from being enriched in mESC LINEs to depleted in rod cell LINEs (fig. S3D and table S2). For the other genomic features, including short interspersed nuclear elements (SINEs), promoters, enhancers, and gene bodies, H3K9me2 shifts from being depleted to enriched or less depleted in the case of promoters (fig. S3D). H3K9me3 is enriched in LINEs and depleted at promoters, enhancers, and gene bodies in both mESCs and rod cells (fig. S3D). Results of principal components analysis (PCA) are also consistent with the notable separation of H3K9me2 and H3K9me3 distributions in the genomes of adult rod cells (fig. S3E). The reversal of H3K9me2 being enriched in peripheral heterochromatin of mESC LADs to being enriched in euchromatin, nonLAD regions of adult rod cells is consistent with the spatial reorganization of chromatin.

H3K9me2-only domains (KODs) remain dimethylated in rod cells

In addition to LADs, H3K9me2 marks other genomic regions located near the nuclear periphery that are not found in LADs as defined by Lamin B chromatin immunoprecipitation sequencing (ChIPseq) or Dam-ID (18, 21). These regions, known as H3K9me2-only domains, or KODs, are enriched for tissue-specific enhancers (19). Although both LADs and KODs contain H3K9me2-modified chromatin in mESCs, we observe notable differences between these domain types in rod cells (Fig. 2A). Unlike cLADs, most KODs remain H3K9me2 modified in adult rod cells (90.6% of all KOD base pairs; Fig. 2B). Similar to nonLADs, when comparing mESCs and rod cells, the H3K9me2 signal increases in most KOD regions, while the H3K9me3 signal decreases (Fig. 2C). The difference between KODs and LADs is also reflected in the enrichment of H3K9me2 in KODs in adult rod cells (1.8-fold observed over expected; fig. S3F). Consistent with the maintenance of the H3K9me2 mark in KODs of adult rod cells, oligoFISH imaging demonstrates that KODs, unlike cLADs, remain at the nuclear periphery (fig. S3G). This finding further supports the likelihood that LADs and KODs are functionally distinct (19).
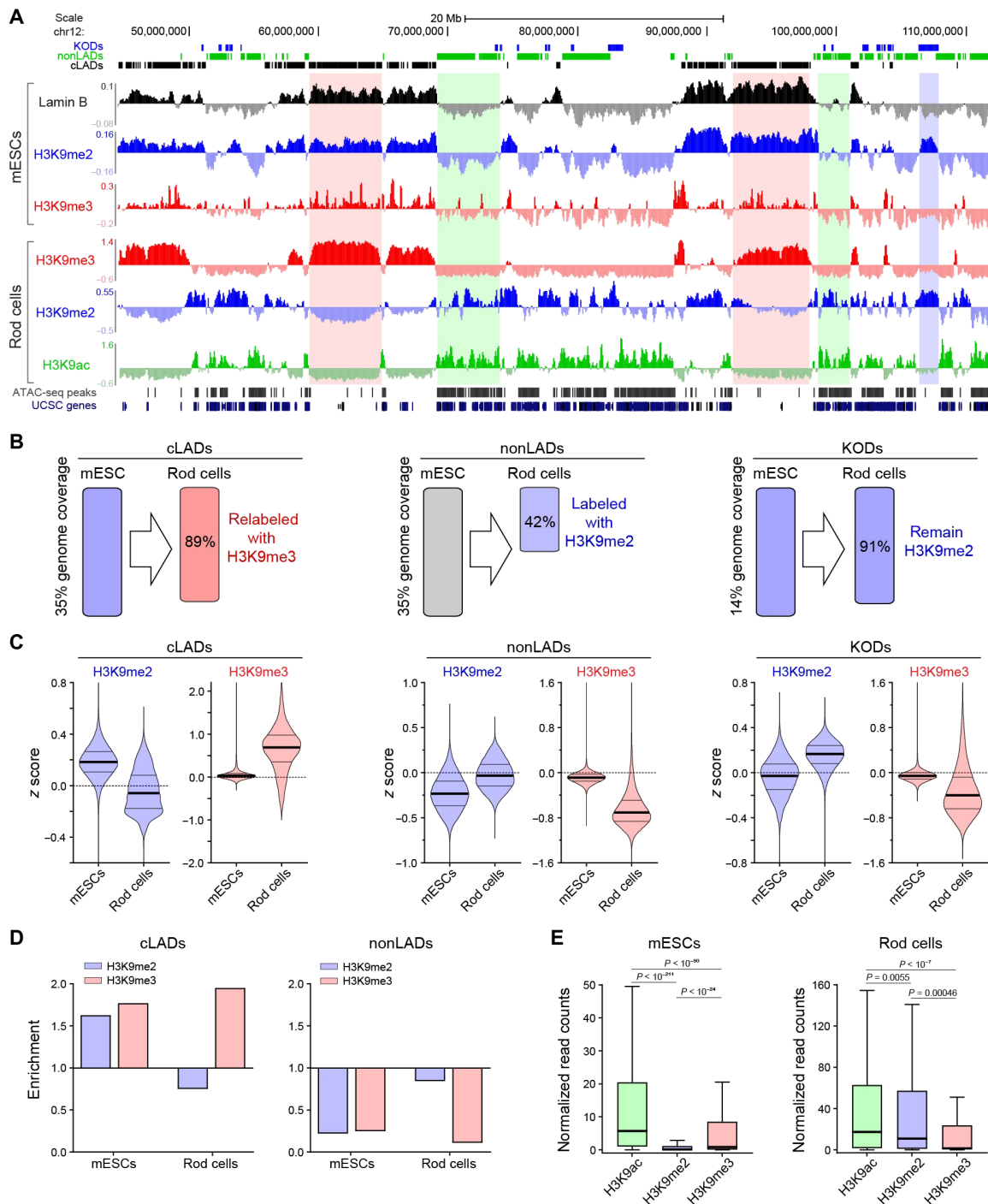
Fig. 2. Spatial chromatin inversion is accompanied by global changes in H3K9 methylation. (**A**) UCSC Genome Browser view (mm10) showing cLADs (black bars), nonLADs (green bars), KODs (blue bars), and representative CUT&RUN tracks for Lamin B (black), H3K9me2 (blue), and H3K9me3 (red) of mESCs; and H3K9me3 (red), H3K9me2 (blue), and H3K9ac (green) for adult rod cells as indicated. ATAC-seq peaks of adult rod cells (*42*) are shown in dark gray, and UCSC genes in blue. Example cLADs (red highlights), nonLADs (green highlights), and KOD (blue highlight) are shown. (**B**) Percent of genome coverage of each indicated domain type and percent of domain coverage associated with H3K9me3 (left) or H3K9me2 (middle and right) for each type in adult rod cells versus mESCs. Blue and red indicate predominantly H3K9me2 and H3K9me3, respectively. (**C**) Distributions of normalized read coverage (*z* score) for H3K9me2 and H3K9me3 histone modifications in domains of each indicated domain type for mESCs and adult rod cells. Lines on violin plots show median, 25th and 75th percentiles. (**D**) Enrichment of H3K9me2 and H3K9me3 in cLADs and nonLADs of mESCs and adult rod cells. (**E**) Transcription of genes with promoters marked by the indicated histone modifications. *y* axes: fragments per kilobase of transcript per million mapped reads (FPKM) values for mESCs (left) and counts per million mapped reads (CPM) values for rod cells (right). Lines on violin plots show median, 25th and 75th percentiles. Box plots show median, 25th and 75th percentiles. Whiskers are drawn using the Tukey method. Statistical analysis for enrichment was performed using GAT with 1000 permutations each (see table S2); all other statistical analysis was performed using analysis of variance (ANOVA) Kruskal-Wallis test with Dunn's multiple comparisons.

H3K9me2, classically considered to be a repressive histone modification (*25*, *26*), has been reported to be a marker of peripheral heterochromatin (*18*) and shown to be essential for localization of chromatin at the nuclear periphery (*20*, *27*). Consistent with a function for H3K9me2 in positioning chromatin at the nuclear periphery, we observed an increase in H3K9me2 modification of euchromatic nonLAD regions in adult rod cells where nonLADs are located at the nuclear periphery. We compared the expression levels of genes with promoters marked by H3K9ac, H3K9me2, and H3K9me3 in mESC and adult rod cells. As expected, we observed active gene expression associated with H3K9ac-marked promoters and repressed expression for genes with H3K9me3-marked promoters in both mESCs and rod cells (Fig. 2E). Unexpectedly, genes with H3K9me2-marked promoters, which are largely repressed in mESCs, are much more likely to be active in rod cells (Fig. 2E and fig. S3H). While there are far fewer H3K9me2-modified promoters than promoters marked by H3K9ac, the associated genes are expressed at comparable levels (Fig. 2E and fig. S3H). This indicates that the H3K9me2 chromatin modification does not confer transcriptional repression in rod cells, although the lack of repression could be rod cell–specific.

Changes in H3K9 methylation occur gradually during postnatal rod cell maturation

The differences in genome-wide H3K9me2 and H3K9me3 histone modifications between mESCs and terminally differentiated, mature rod photoreceptors are notable. To compare histone modifications of adult rod cells with rod cells just before nuclear inversion, we monitored epigenetic changes in rod cells during progressive stages of postnatal development. Lineage specification of rod photoreceptors occurs between embryonic day 14 (E14) and postnatal day 6 (P6), at which point rod cells exit the cell cycle (*12*). Postmitotic rod cells further mature between P6 and P28, and it is during this period that rod nuclei undergo spatial inversion (*10*). We performed H3K9me2 and H3K9me3 CUT&RUN on flow-sorted rod cells isolated from P1, P7, P14, and P21 mice (Fig. 3A). We observed few differences in H3K9me2- and H3K9me3-marked chromatin regions between mESCs and immature rod cells isolated at either P1 or P7 (Fig. 3). However, between P7 and P21, progressive changes in both H3K9me2 and H3K9me3 coverage became apparent across the genome, most notably in cLADs and nonLADs (Fig. 3). At P14, approximately 35% of the regions that will be relabeled by adulthood show H3K9me2/me3 relabeling, and more than 80% relabeling occurs by P21 (fig. S4A). These results indicate that the majority of histone H3K9 relabeling in both cLAD and nonLAD regions occurs concurrently and gradually between P7 and P21. We observed a lack of mitotic features in retinal cells collected at P7 and later (fig. S4B), consistent with previous observations that rod cells exit the cell cycle around P6 (*12*). These results suggest that lineage specification of rod cells, which happens between E13 and P6 (*11*, *12*), is independent of chromatin relabeling and spatial chromatin inversion, which occur after P7 (Figs. 3 and 4).

As noted above, KOD regions, unlike cLADs, largely maintain dimethylation at H3K9 and even show an increase in most regions by P21 (Fig. 3, B and C, and fig. S4C). This is accompanied by a gradual loss of H3K9me3 in KODs as is also observed in nonLAD regions (Fig. 3, B to E). Although both LADs and KODs are H3K9me2-modified chromatin at the nuclear periphery of conventionally organized nuclei, we observed a selective H3 Lys9 trimethylation of cLADs but not KODs during rod cell maturation. Both KODs and nonLADs display a progressive increase of H3K9me2 and loss of H3K9me3 (Fig. 3). This is consistent with a role for H3K9me2 as a positional mark that is associated with chromatin at the nuclear periphery.

Spatial reorganization of chromatin occurs in parallel with H3K9 relabeling

Previous studies demonstrated that spatial rearrangement of heterochromatin and euchromatin in the nuclei of rod cells occurs during the postnatal period between P1 and P28 (*8*), and our CUT&RUN data show that chromatin relabeling is most dynamic between P7 and P21 (Figs. 3 and 4A). We examined the localization of multiple genomic loci representing cLADs and nonLADs, in rod cells isolated at P1 to P28, at the same time as they were undergoing changes in H3K9me2/me3 methylation (Fig. 4B). Retinal cells were isolated from P1, P7, P14, P21, and P28 mice and hybridized with oligoFISH probes targeting a representative set of 41 cLADs and 41 nonLADs [table S1; (*20*)]. In P1 and P7 rod cells, we found that these loci maintain their conventional positioning, with cLADs at the nuclear periphery and nonLADs in the nuclear interior (Fig. 4B). This observation is consistent with our CUT&RUN data, which revealed no major differences in H3K9me2/me3 methylation between mESCs and P1 or P7 rod cells (Fig. 3). In rod cells isolated at P14, we observed an intermediate localization of cLADs and nonLADs, with both groups of probes distributed throughout the nucleus (Fig. 4B). By P21, there was a significant and almost complete inversion of spatial positioning, with a majority of nonLADs having moved to the nuclear periphery and cLADs located in the nuclear interior (Fig. 4B). In P28 rod cells, localization of cLADs and nonLADs is similar to that of adult rod cells (Figs. 1D and 4B). These data demonstrate that spatial repositioning of heterochromatic cLAD and euchromatic nonLAD regions happens gradually between P7 and P21 and, together with the CUT&RUN results, indicate that chromatin relabeling and spatial inversion occur in parallel over a period of 2 weeks in the postnatal mouse rod photoreceptor.

Because our genome-wide CUT&RUN data showed that KODs maintain their H3K9me2 modification and are not relabeled with H3K9me3 in mature rod cells (Figs. 2B and 3C), we also examined the position of 10 KOD regions in individual rod cells using oligoFISH probes. We found that the majority of KODs did not undergo marked positional changes but remain localized at the nuclear periphery in rod cells even while these cells transition from conventional to inverted nuclear architecture (Fig. 4C).

Next, we used immunofluorescent staining to examine the patterns and localization of H3K9me2-, H3K9me3-, and acetyl–H3 histone–modified chromatin in rod cells from P1 to P28 (Fig. 4D). We did not observe any major changes in the staining patterns of any of these marks between P1 and P7. At P14, H3K9me3-marked heterochromatin (dense DAPI staining) was observed to be detached from the nuclear periphery and organized around chromocenters. By P21, these regions form two large heterochromatin domains that then fuse into one centrally located heterochromatin mass by P28. Similarly, at P14, acetyl-H3–marked euchromatin is located between large heterochromatin compartments and at the nuclear periphery. By P21, the acetyl-H3–modified euchromatin is found mainly at the nuclear periphery, with a small lagging portion at the border of the two heterochromatin regions (Fig. 4D). The H3K9me2 histone modification was consistently observed at the nuclear periphery at all stages of rod cell maturation and nuclear inversion (Fig. 4D). We note that, at P14,
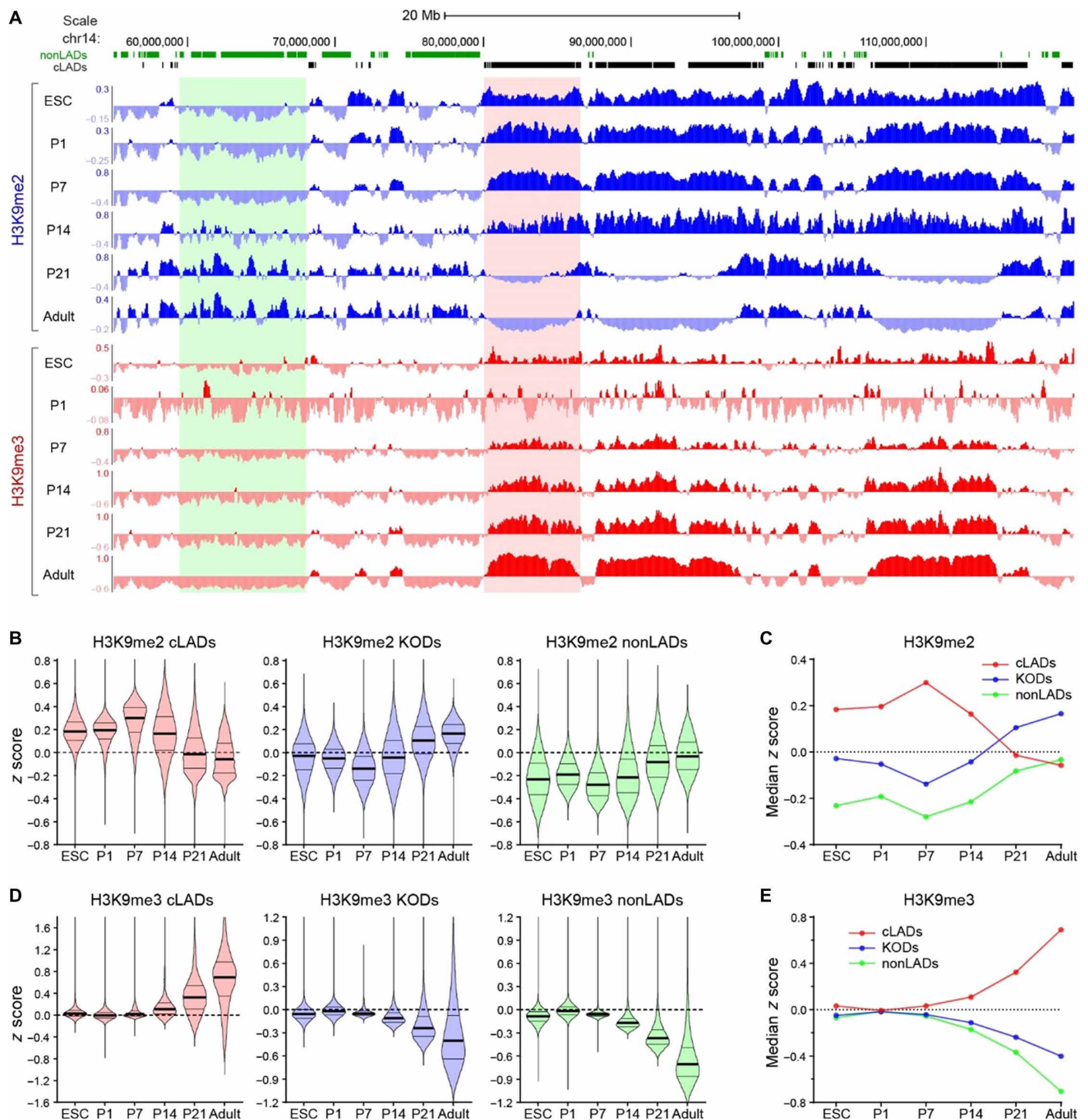
Fig. 3. Changes in H3K9 methylation occur gradually during postnatal rod cell maturation. (**A**) UCSC Genome Browser view (mm10) showing cLADs (black bars), non-LADs (green bars), and representative CUT&RUN tracks for H3K9me2 (blue) and H3K9me3 (red) in mESCs and at indicated time points of rod cell maturation. An example cLAD (red highlight) and nonLAD (green highlight) are shown. (**B**) Distributions of normalized read coverage (z score) of H3K9me2 histone modification for genomic regions of indicated domain types compared between mESCs, and postnatal and adult rod cells. (**C**) Median read coverage (z score) of H3K9me2 histone modification for all genomic regions of indicated domain types for mESCs, and postnatal and adult rod cells. (**D**) Distributions of normalized read coverage (z score) of H3K9me3 histone modification for genomic regions of indicated domain types from mESCs, and postnatal and adult rod cells. (**E**) Median read coverage (z score) of H3K9me3 histone modification for all genomic regions of indicated domain types for mESCs, and postnatal and adult rod cells. Lines on violin plots show median, 25th and 75th percentiles.
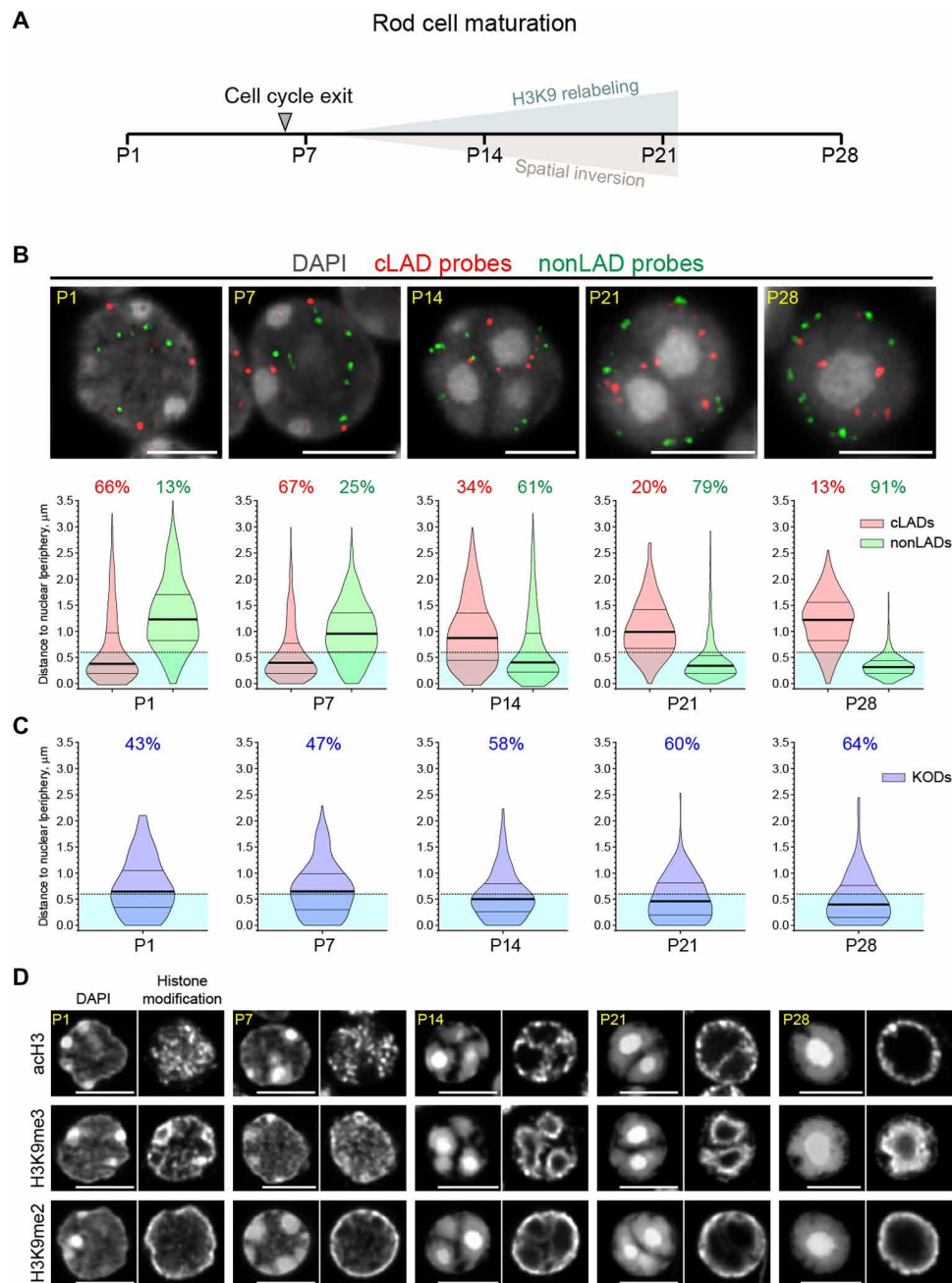
Fig. 4. Spatial reorganization of chromatin occurs in parallel with H3K9 relabeling in maturing rod cells. (**A**) A schematic representation of rod photoreceptor maturation from P1 to P28. (**B**) Representative confocal images (top) of rod cells hybridized with fluorescent DNA oligoFISH probes targeting cLADs (red) and nonLADs (green) shown at indicated time points. Counterstained with DAPI (gray). Violin plots (bottom) show distributions of distances to the nuclear periphery of individual cLAD (red) and nonLAD (green) probes. $n = 25$ cells, minimum 400 loci. (**C**) Violin plots show distributions of distances to the nuclear periphery of KOD probes. $n = 25$ cells, minimum 160 loci. (**D**) Representative immunofluorescent confocal images of rod cells at indicated time points stained for indicated histone modification and counterstained with DAPI. For (B) and (C), dotted lines indicate average thickness of H3K9me2 peripheral chromatin layer, and the peripheral zone is highlighted (light blue). Lines on violin plots show median, 25th and 75th percentiles. Percent of cLAD, nonLAD, and KOD loci at the nuclear periphery (within average thickness of peripheral chromatin) is shown above violin plots. Scale bars, 5 μm.

a small portion of weakly H3K9me2-staining chromatin colocalizes with DAPI staining regions (commonly marked with H3K9me3) away from the nuclear periphery (Fig. 4D). We propose that this may be an intermediate state, as LADs undergo relabeling from H3K9me2 to H3K9me3 and are released from the nuclear periphery.

Changes in H3 Lys9 methylation correlate with changes in spatial positioning

The combined results of immunostaining and oligoFISH suggest that most rod cells in a given population proceed fairly uniformly through maturation and demonstrate a similar degree of chromatin spatial

inversion and histone relabeling at all time points examined from P1 to P28. To assess the heterogeneity in localization for the individual genomic loci across cells at a given stage of the maturation process, we plotted the distance to the nuclear periphery for each cLAD and nonLAD probe, in each individual cell, at each time point, P1 to P28 (Fig. 5A). P1 and P7 rod cells display conventional nuclear organization, with cLADs at the nuclear periphery and nonLADs broadly distributed throughout nuclear interior (Fig. 5A). That pattern is reversed for P21 and P28 rod cells, when nonLADs are observed to be almost uniformly positioned near the nuclear periphery, and LADs have moved away from the periphery and occupy more widely variable positions outside of the nuclear peripheral zone. For each genomic locus represented by a cLAD and nonLAD probe, we calculated the average normalized coverage across the region for H3K9me2 and H3K9me3 modifications. We compared the relative amount of each modification at each cLAD and nonLAD region over the course of rod cell maturation, from P1 through adult rod cells (Fig. 5B). For both LADs and nonLADs, we observe changes in H3 Lys9 methylation that correspond with changes in spatial positioning at nearly every locus assayed. Overall, the distance to the nuclear periphery is negatively correlated with the amount of H3K9me2 and positively correlated with the amount of H3K9me3 [Pearson r values for cLADs: −0.92 (with H3K9me2) and +0.93 (with H3K9me3); nonLADs: −0.65 (with H3K9me2) and +0.76 (with H3K9me3)]. Together, these results demonstrate that epigenetic relabeling and spatial chromatin repositioning of individual loci occur in parallel during rod cell maturation. Overall, this study reveals that rod cells undergo a global epigenetic relabeling and concomitant spatial reorganization of chromatin to achieve the specialized properties of the adult nocturnal mammalian rod cell nucleus.

DISCUSSION

Our findings demonstrate that the spatial reorganization of chromatin in murine rod photoreceptor cells is accompanied by global epigenetic relabeling of the genome. Heterochromatin, including that found at the nuclear periphery in LADs, is repositioned to the center of the nucleus in adult murine rod cells. The H3K9me2 histone modification that marks peripheral chromatin of LADs in cells with conventional nuclear organization, including retinal precursor cells, is replaced with H3K9me3 in inverted nuclei of mouse rod photoreceptors. This coincides with the repositioning of heterochromatin to the center of the nuclei. In contrast, the H3K9me2 mark, which is rare in euchromatic nonLAD regions of conventionally organized nuclei, is much more common in euchromatin regions relocated to the nuclear periphery of inverted rod cells. This H3K9me2 enrichment suggests a role for H3K9me2 in chromatin organization at the nuclear periphery and indicates that H3K9me2 is not restricted in all cases to heterochromatin. Rather, it is restricted to the nuclear periphery.

Our work also shows that KODs, which were recently reported as H3K9me2-labeled peripheral chromatin regions with minimal Lamin B contact in conventionally organized nuclei (19), maintain both the H3K9me2 mark and peripheral localization during all steps of rod cell maturation, despite the global rearrangement of all other chromatin domains that occurs during inversion. This is consistent with a role for H3K9me2 as a spatial positioning mark for peripheral chromatin. Together, our results suggest that there is a critical interdependence of the epigenetic state of chromatin and its spatial localization and organization. Specifically, we demonstrate that spatial

repositioning of chromatin is accompanied by changes in H3K9 methylation (Fig. 6). Given the unique genome-wide epigenetic transformation coupled with a global spatial repositioning of chromatin, the murine rod cell presents a unique model in which to study the role of histone modifications in chromatin organization. Rod cell maturation, which can occur ex vivo, offers an exquisite opportunity to investigate the molecular mechanisms involved in chromatin relabeling, condensation, and spatial positioning.

Previous studies uncovered a role for chromatin organizers and tethers in establishing the inverted nuclear architecture of mouse rod cells. LBR and Lamin A/C participate in the tethering of heterochromatin to the nuclear periphery in conventionally organized nuclei but are not expressed in mature rod cells (10). Loss of LBR and Lamin A/C expression was shown to be essential for release of H3K9me3- and H4K20me3-marked heterochromatin from the nuclear periphery (10, 17). Lamin A/C is absent in rod cell precursors, so its absence in mature rod cells cannot alone account for the inversion of chromatin, and Lamin A/C and LBR may serve redundant functions in heterochromatin tethering in cells with conventional nuclear architecture. The absence of both Lamin A/C and LBR in nonretinal cells results in significant heterochromatin condensation in the nuclei interior, but euchromatin is not restricted to the nuclear periphery (10). Thus, LBR- and Lamin A/C–null cells cannot fully achieve the inverted nuclear organization observed in rod cells. Our results suggest a role for histone relabeling in the repositioning of de novo H3K9me3-marked LADs from the nuclear periphery to the center of the nucleus and for repositioning of de novo H3K9me2-marked euchromatin to the periphery. Together, cell type–specific absence of H3K9me3 chromatin tethers is likely to work in concert with epigenetic relabeling to enable chromatin inversion in rod cells.

While the inverted nuclear architecture of rod cells in nocturnal animals sets them apart from all other cells with conventionally organized nuclear architecture, a recent study showed that the overall euchromatin and heterochromatin domain organization, chromatin compartments, and interactions between topologically associating domains (TADs) observed in conventional nuclei are maintained in murine rod cells (14). This suggests that replacement of H3K9me2 with H3K9me3 in LADs and increased H3K9me2 modification of euchromatin does not alter genome-wide 3D interactions within and between chromatin compartments but affects primarily the positioning of the genome inside the nucleus.

H3K9me2 and H3K9me3 histone modifications, which mark heterochromatin and partially overlap in conventional nuclei, become separated in mature rod cells as observed both by microscopy (Figs. 1 and 4) and genomic analysis (fig. S3, D and E). This is consistent with a model in which H3K9me2 serves as a positional mark for peripheral chromatin. In contrast, H3K9me3 may organize heterochromatin in the nuclear interior. A loss of H3K9me3 from euchromatic regions (Fig. 2 and fig. S3D) may be required for spatial separation of H3K9me2-marked euchromatin at the nuclear periphery and H3K9me3-marked heterochromatin in the nuclear interior. Historically, H3K9me2 and H3K9me3 histone modifications have been regarded as related repressive chromatin marks with potentially overlapping functions (often referred to as "H3K9me2/3") (28–31), but recent research has revealed cellular mechanisms that can differentiate dimethyl from trimethyl groups on H3K36 histone lysine residues and their distinct biological functions (32). While partial nuclear localization differences between H3K9me2 and H3K9me3 have been reported previously (18), both histone modifications are observed at the nuclear periphery
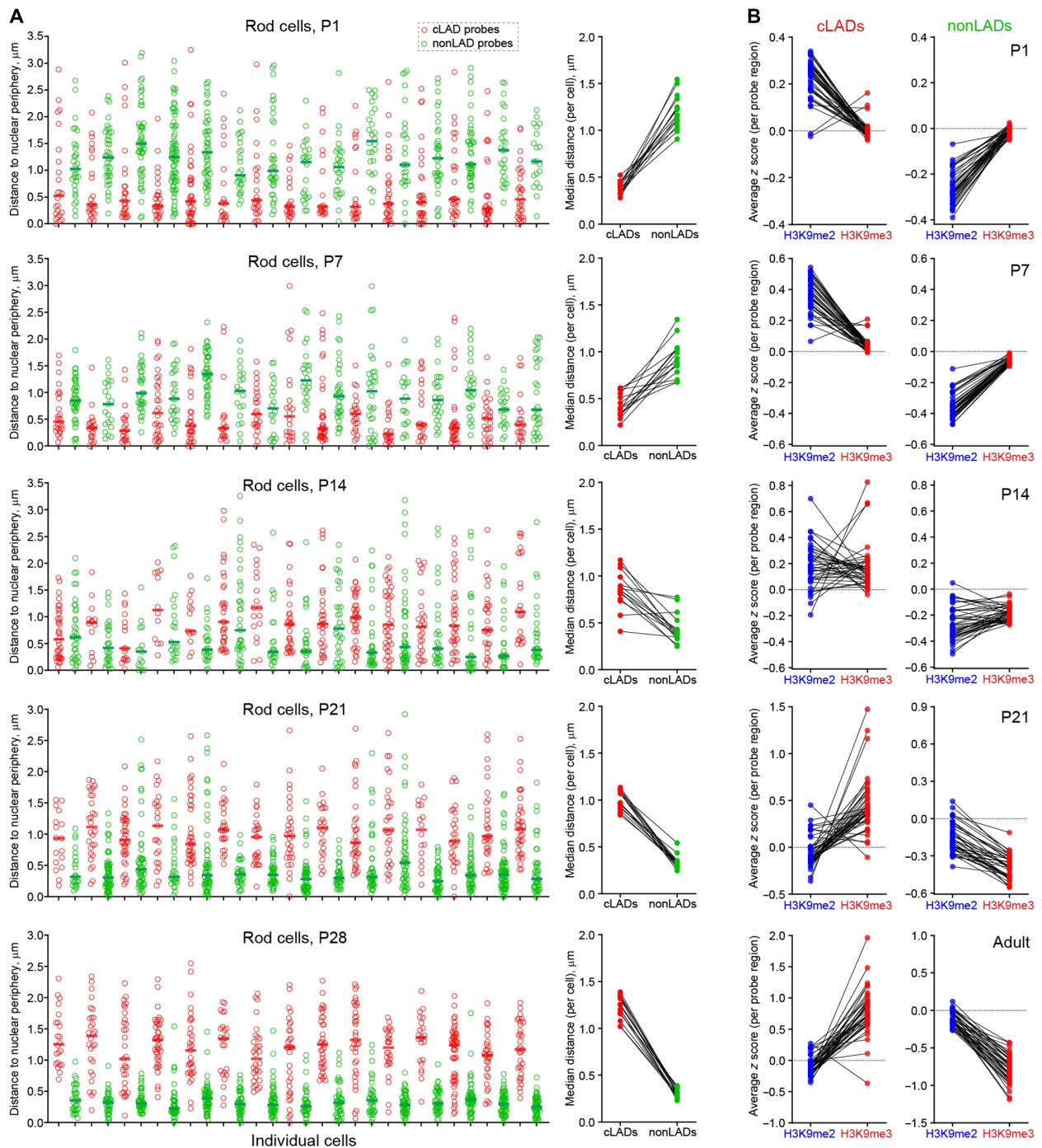
Fig. 5. Individual genomic loci reflect parallel changes in spatial repositioning and chromatin relabeling during rod cell maturation. (**A**) Dot plots (left) show distribution of distances to the nuclear periphery (as defined by Lamin B) for individual cLAD (red) and nonLAD (green) probes in individual rod cells at indicated postnatal day; red and green lines indicate median values. Dot plots (right) show median distances to the nuclear periphery for cLAD (red) and nonLAD (green) probes in each cell. Lines connect values that belong to the same cells. *n* = 15 cells. (**B**) Dot plots show average read coverage (z score) for H3K9me2 (blue) and H3K9me3 (red) for each cLAD (left) and nonLAD (right) region targeted with oligoFISH probes in the population at each time point. Lines connect values that belong to the same regions. *n* = 41 cLAD and 41 nonLAD probes.

in conventionally organized nuclei, making it difficult to distinguish unique functions in peripheral tethering. Our findings in rod cells demonstrate that H3K9me2- and H3K9me3-marked chromatin can be spatially separated, suggesting that the cell has mechanisms to distinguish di- from trimethylation on H3K9, thereby enabling independent organization of these two classes of chromatin.

Our results indicate that H3K9me2-marked peripheral chromatin can be selectively recognized and either relabeled with H3K9me3, as in the case of cLADs, or remain H3K9me2-modified, as in KODs. This suggests that H3K9me2-modified chromatin must be specified, with additional distinctive histone modifications or by other factors, such that one chromatin type (LADs versus KODs) can be "read" as
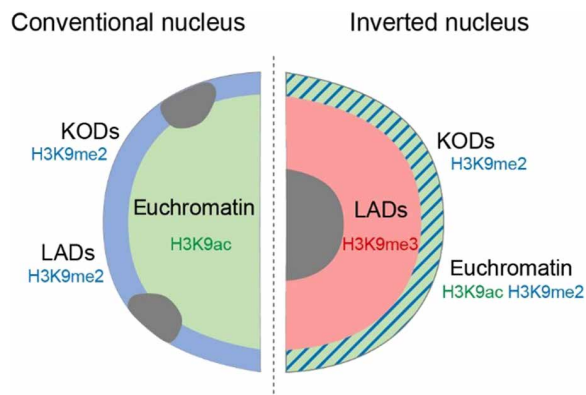
Fig. 6. A model of chromatin reorganization in murine rod photoreceptors. Spatial chromatin inversion in rod cells is accompanied by changes of histone H3K9 methylation status. During rod cell maturation, as nuclear architecture transitions from conventional to inverted, H3K9me2-marked heterochromatin regions of LADs are relabeled with H3K9me3 and repositioned from the nuclear periphery to the nuclear interior. Centrally localized euchromatin regions are labeled with H3K9me2 and repositioned to the nuclear periphery. Specialized genomic regions like KODs maintain H3K9me2 and remain near the nuclear periphery in both conventional and inverted nuclei. H3K9me2 marks chromatin at the nuclear periphery in both conventional and inverted nuclei.

different from the other. Similarly, the cellular mechanisms that orchestrate histone relabeling in rod cells must operate in a way that allows regions like cLADs, which start out as H3K9me2 marked before inversion, to be distinguished from other genomic regions, like euchromatin, which acquire new H3K9me2 by P14. Further studies are required to identify the molecular mechanisms that provide such selectivity on a global level.

It was unexpected to find H3K9me2 at euchromatic nonLAD regions in rod cells, because H3K9me2 has traditionally been considered a repressive histone modification (*18*, *25*, *29*, *31*, *33*). However, recent studies offer evidence that H3K9me2 functions in the organization of chromatin at the nuclear periphery. H3K9me2 has been shown to "bookmark" chromatin for peripheral localization (*20*), and ectopic addition of H3K9me2 promotes repositioning of a genomic region from the nuclear interior to the periphery (*27*). A role for H3K9me2 in spatial positioning is consistent with the observed gain of H3K9me2-modified histones in euchromatic regions at the nuclear periphery of rod cells. While H3K9me2 may be passively repressive (i.e., methylation at this lysine residue must be removed before acetylation), we predict that H3K9me2 does not have a direct repressive function in adult rod cells. This hypothesis is supported by the observation of active transcription from H3K9me2-marked promoters in rod cells (Fig. 2E). The H3K9me2-marked euchromatin of inverted rod cells spans mainly intergenic regions and does not appear to form large chromatin domains. Furthermore, a putative H3K9me2-tethering complex might normally include a specific repressive component that is not expressed in rod cells.

The fact that H3K9me2-marked peripheral euchromatin and H3K9me3-marked heterochromatin are organized separately and are spatially segregated in rod cells suggests that both histone modifications may contribute directly to chromatin spatial rearrangement in rod cells. This is consistent with our observations of dense heterochromatin at the nuclear periphery gaining H3K9me3 and being released

from the periphery due to lack of H3K9me3 tethers and then condensing into a large heterochromatin mass in the center of the nucleus. At the same time, chromatin regions that maintain H3K9me2 (KODs) persist at the nuclear periphery, and euchromatin regions gain H3K9me2 and are repositioned at the nuclear periphery. Further studies are required to fully elucidate the mechanisms behind such global reprograming of the genome, but chromatin inversion in rod photoreceptors provides a unique and attractive model for studying epigenetic regulation of chromatin organization.

METHODS

Cell lines and primary cells

Murine embryonic multipotent stem cells [American Type Culture Collection (ATCC), cat. no. CRL-1934, RRID:CVCL_4378] were obtained from the ATCC. Cells were tested negative for mycoplasma contamination. mESCs were maintained at 37°C; cultured in Dulbecco's modified Eagle's medium (Corning, cat. no. 10-013-CV) and 15% fetal bovine serum (Fisher Scientific, cat. no. SH3007003), 1 mM sodium pyruvate (Thermo Fisher Scientific, cat. no. 11360070), MEM Non-Essential Amino Acids Solution (Invitrogen, cat. no. 11140050), 50 mM β-mercaptoethanol (Thermo Fisher Scientific, cat. no. 21985023), penicillin-streptomycin (10,000 U/ml; Thermo Fisher Scientific, cat. no. 15140122), and ESGRO leukemia inhibitory factor (1000 U/ml; EMD Millipore, cat. no. ESG1106); and supplemented with 1 μM MEK inhibitor PD0325901 (Sigma-Aldrich, cat. no. PZ0162) and 3 μM GSK3 inhibitor CH99021 (Sigma-Aldrich, cat. no. SML1046). Primary retina cells were isolated from C57BL/6 mice obtained from Charles River Production. This study complied with all relevant ethical regulations, and all mouse protocols were approved by the University of Pennsylvania Institutional Animal Care and Use Committee.

Primary cell isolation and cell sorting

Retinal cells were isolated using a papain isolation kit (Worthington Biochemical Corporation, cat. no. LK003150). Isolation protocol was adopted from the manufacturer's recommendations and previously published (*34*). Retina tissue was isolated and incubated with papain solution for 24 to 30 min at 37°C with 600 revolutions per minute in a thermal shaker (VWR, cat. no. 89232-908), and then papain was blocked with a blocking solution. For CUT&RUN assays, live retina cells isolated from postnatal animals at days 7, 14, and 21, and adult animals were flow sorted using forward scatter (FSC) and side scatter (SSC) plot as previously described (*34*). Sorted population was immunostained for rhodopsin, a marker of rod photoreceptor cells (fig. S2). For immunofluorescence and oligoFISH, retinal cells were fixed with 2% paraformaldehyde (PFA) (Electron Microscopy Sciences, cat. no. 15710) and spun down on poly-L-lysine–treated coverslips at 1000g in cushion buffer [100 mM KCl, 1 mM MgCl$_2$, 0.1 mM CaCl$_2$, 250 mM sucrose, 10 mM Hepes (pH 7.4), and 25% glycerol].

Immunofluorescence

The following procedures were previously described (*20*). Primary mouse retinal cells and undifferentiated embryonic stem cells were fixed with 2% PFA (EMS, cat. no. 15710) for 10 min at room temperature (RT), washed three times with Dulbecco's phosphate-buffered saline (DPBS) (Gibco, cat. no. 14190-136), and then permeabilized with 0.25% Triton X-100 (Thermo Fisher Scientific, cat. no. 28314) for 10 min. After permeabilization, cells were washed three times with DPBS for 5 min and then blocked in 1% bovine serum albumin

(Sigma-Aldrich, cat. no. A4503) in PBST [DPBS with 0.05% Tween 20; pH 7.4 (Thermo Scientific, cat. no. 28320)] for 30 to 60 min at RT; incubated with primary antibodies for 1 hour at RT and then washed three times with PBST for 5 min; and incubated with secondary antibodies for 30 to 60 min at RT and then washed two times with PBST for 5 min. Cells were counterstained with DAPI solution (Sigma-Aldrich, cat. no. D9542) for 10 min at RT and then rinsed with PBS. Coverslips were mounted on slides using 80% glycerol mounting medium: 80% glycerol (Invitrogen, cat. no. 15514-011), 0.1% sodium azide (Sigma-Aldrich, cat. no. S2002), 0.5% propyl gallate (Sigma-Aldrich, cat. no. 02370), and 20 mM tris-HCl (pH 8.0) (Invitrogen, cat. no. 15568-025).

Immunofluorescence and DNA oligoFISH
The following procedures were previously described (20). mESCs were grown on 0.1% porcine gelatin (Sigma-Aldrich, cat. no. G2500)–coated glass coverslips (EMS, cat. no. 3406) and fixed with 2% PFA for 10 min at RT. Then, cells were immunostained as described above. DNA oligo hybridization protocol was described before (20). In brief, after incubation with secondary antibodies, samples were washed with DPBS and postfixed with 2% PFA for 10 min at RT, washed three times with DPBS and permeabilized with 0.7% Triton X-100 for 10 min at RT, and then rinsed with DPBS. Coverslips were incubated in 70, 90, and 100% ethanol for 2 min each and then washed in 2× SSC (Corning, cat. no. 46-020-CM) for 5 min. Coverslips were equilibrated in 2× SSCT (2× SSC with 0.1% Tween 20) with 50% formamide for 5 min at RT. DNA denaturation was performed in 2× SSCT with 50% formamide for 2 to 3 min at 92°C in water bath and then additional 20 min at 60°C in water bath. After DNA denaturation, coverslips were cooled to RT in humid conditions for 2 to 3 min. Coverslips were places on a slide with 10 to 20 μl of hybridization mix (50% formamide, 10% dextran sulfate, and 50 to 100 pmol of primary DNA oligo probes). Coverslips were heated at 92°C for 3 min on a heat block and then incubated overnight at 37°C in a humid chamber. After hybridization with primary DNA oligo probes, coverslips were washed in 2× SSCT for 15 min at 60°C, then for 10 min in 2× SSCT for 10 min at RT, and then transferred in 2× SSC for 5 min. Next, coverslips were hybridized with a secondary fluorescent DNA oligo probes (10% formamide, 10% dextran sulfate, and 10 pmol of secondary DNA probes) in dark humidified chamber for 3 hours at RT. After secondary hybridization, coverslips were washed for 5 min in 2× SSCT at 60°C, then 2× SSCT at RT, and 2× SSC buffer with DAPI. Samples were rinsed with DPBS and mounted on a slide as described above.

Antibodies
Antibodies used in this study: H3K9me2 (Active Motif, cat. no. 39239, RRID:AB_2793199), H3K9me3 (Abcam, cat. no. ab8898, RRID:AB_306848), acetyl-H3 (Millipore, cat. no. 06-599, RRID:AB_2115283), acetyl-H4 (Millipore, cat. no. 06-866, RRID:AB_310270), H3K9ac (Active Motif, cat. no. 61251, RRID:AB_2793569), H3K9ac (Active Motif, cat. no. 39137, RID:AB_2561017), H3K9me2S10P (Active Motif, cat. no. 61429, RRID:AB_2793632), Lamin B1 (Abcam, cat. no. ab16048, RRID:AB_10107828), Lamin B (Santa Cruz Biotechnology, cat. no. sc-6217, RRID:AB_648158), Lamin A/C (Santa Cruz Biotechnology, cat. no. sc-376248, RRID:AB_10991536), anti-rhodopsin (Santa Cruz Biotechnology, cat. no. ab98887, RID:AB_10696805), and rabbit normal immunoglobulin G (IgG) (Cell Signaling Technology, cat. no. 2729s, RRID:AB_1031062). Antibodies against H3K9me2 (Active Motif, cat. no. 39239) and H3K9me3 (Abcam, cat. no. ab8898) were tested for specificity previously (18, 20).

Image acquisition and analysis
The following procedures were previously described (20). All confocal immunofluorescent and oligoFISH images were taken with a Leica TCS SP8 and SP8 3× STED confocal microscopes using 63×/1.40 oil objective. DAPI staining (blue channel) was acquired using a photomultiplier tube detector with offset −0.1% or hybrid detector (HyD) in the standard mode with 100% gain. All other fluorescent staining (green, red, and far red channels) were acquired using HyDs in the standard mode with 100% gain. All images were taken with minimal laser power to avoid saturation. 3D images were taken as z stacks with 0.05-μm intervals with an average of 100 z planes per nucleus. Confocal 3D images were deconvoluted using Huygens Professional software using the microscope parameters, standard point spread function, and automatic settings for background estimation. Confocal channel shift alignment was performed using 0.1 μm of TetraSpeck fluorescent beads (Invitrogen, cat. no. T7279). 3D image reconstructions were performed using Imaris 9.0.1 software (Bitplane AG, Switzerland) as described previously (18, 20). Briefly, nuclear lamina, nuclear DNA volume, and H3K9me2-marked chromatin structures were created using Surfaces tool with automatic settings based on the fluorescent signals from the anti–Lamin B, DAPI staining, and anti-H3K9me2 antibodies. DNA oligoFISH probe spots were identified using the Spots tool with a diameter of 300 nm, created at the intensity mass center of the fluorescent probe signal. Distance from the center of the DNA oligoFISH spot to the edge of the nuclear lamina surface was quantified using the Distance Transformation cool. The distances were corrected by the average distance of chromatin embedment in the nuclear lamina surface. If the distance from the DNA oligoFISH spot to the nuclear lamina was smaller than (or equal to) the average thickness of peripheral chromatin, then the spot was counted as localized at the nuclear periphery. The average thickness of the H3K9me2-marked peripheral chromatin layer in mESC was measured previously (18, 20) and equals 0.6 μm.

Cleavage under target and release using nuclease (CUT&RUN)
The CUT&RUN protocol was performed as previously described (35) with modifications. Briefly, 1×10^6 cells (mESCs, retina cells, or rod cells isolated as described above) were harvested and washed twice with ice-cold PBS. Nuclei were isolated with nuclear extraction buffer [20 mM Hepes-KOH (pH 7.9), 10 mM KCl, 0.5 mM spermidine (Sigma-Aldrich, cat. no. 05292-1 ml-F), 0.1% Triton X-100, 20% glycerol, and 1× protease and phosphatase inhibitor (Thermo Fisher Scientific, cat. no. 78442)]. To aid in nuclear capture, isolated nuclei were incubated with activated concanavalin A beads (Bangs Laboratories, cat. no. Bp531) for 15 min at RT followed by incubation with the primary antibody or IgG control (1:100 dilution) overnight. Unbound antibody was removed with Wash Buffer [20 mM Hepes-NaOH (pH 7.5), 150 mM NaCl, 0.5 mM spermidine, and 1× protease phosphatase inhibitor] for a total of two washes. Supernatant was removed following bead-liquid separation using a magnetic stand and the fusion of protein A–micrococcal nuclease (pA-MNase; batch 6; stock concentration, 143 μg/ml) was added at a final concentration of 700 ng/ml. The complex was incubated for 1 hour at 4°C. Following incubation, the bound complexes were washed twice with Wash Buffer and placed in a 0°C metal block for 5 min to prechill the tubes. To activate pA-MNase, $CaCl_2$ was added to the prechilled bound complexes at a final concentration of 2 mM and incubated in the 0°C metal block for 30 min. The digestion reaction was neutralized by the addition of an equal volume of 2× STOP buffer (200 mM NaCl, 20 mM EDTA, 4 mM EGTA, 50 μg/ml ribonuclease A, and

40 µg/ml glycogen) followed by incubation at 37°C for 10 min to release cleaved DNA fragments. The targeted protein-DNA complex was released via centrifugation at 16,000g for 5 min, and supernatant was collected and transferred to freshly labeled 1.7-ml LoBind tubes. Digested DNA was purified via spin column (Macherey-Nagel, cat. no. 740609.250) according to the manufacturer's instructions to recover large DNA-protein complexes. DNA concentration was estimated using the Qubit fluorometer, and quality was assessed before library preparation using the Agilent Bioanalyzer 2100 (Agilent Technologies, USA) using the High Sensitivity DNA Kit (Agilent Technologies, cat. no. 5067-4626). pA-MNase (batch 6) was provided by S. Henikoff. The antibodies used were rabbit polyclonal anti-H3K9me2 (Active Motif, cat. no. 39239), rabbit polyclonal anti-H3K9me3 (Abcam, cat. no. ab8898), rabbit polyclonal anti–Lamin B 1 (Abcam, cat. no. 16048), rabbit polyclonal anti-H3K9ac (Active Motif, cat. no. 39137), and normal rabbit IgG (Cell Signaling Technology, cat. no. 2729s).

Library preparation for CUT&RUN
Construction of the CUT&RUN DNA libraries for next-generation sequencing was carried out with modifications using the KAPA HyperPrep Kit (Kapa Biosystems, no. KK8502 07962347001), coupled with the NEBNext Multiplex Oligos for Illumina [New England Biolabs (NEB), no. E6440S]. Briefly, the end repair and A-tailing temperature was dropped from the recommended 65° to 58°C to avoid denaturation of small AT-rich fragments, and the reaction time for this step was increased to 60 min to compensate for lower enzymatic activity. Adapter ligation was performed using the NEB adapter stock diluted to the desired concentration. Following adapter ligation, the manufacturer-recommended volume of NEB USER enzyme was added to the reaction and incubated at 37°C for 15 min to ensure digestion of the uracil bridge, allowing successful pairing of the primers containing barcodes in the successive steps of the reaction. After adapter ligation and hairpin cleavage, 1.1× Agencourt AMPure Beads (Beckman Coulter, cat. no. A63880) were added to the reaction to ensure high recovery of short- to medium-sized fragments. For the amplification reaction, 10 µl of the NEBNext Multiplex Oligos were added to the samples, replacing the KAPA Library Amplification Primer Mix (10×), and subjected to 14 cycles of amplification. Postamplification cleanup was carried out using 1.1× Agencourt AMPure Beads. The libraries were quantified via quantitative polymerase chain reaction using the KAPA Library Quantification Kit for Illumina Platforms (Kapa Biosystems, cat. no. KK4835 07960204001), and quality control was carried out on the Agilent Bioanalyzer 2100 Expert (Agilent Technologies, USA) using the High Sensitivity DNA Kit (Agilent Technologies, cat. no. 5067-4626). Barcoded libraries were quantified and pooled together in equimolar ratio. The pooled libraries were denatured according to the standard Illumina protocol. Samples were paired-end sequenced on the Illumina NextSeq 500/550 platform [2 × 36 base pairs (bp), 75 total cycles] (Illumina, cat. no. 20024906).

Sequencing analysis
Paired-end reads were aligned against reference genome (mm10) using Bowtie2 version 2.2.5 (36) with default parameters "-X 2000 -N 1 --local --dovetail." Only properly paired, primary alignments were kept for downstream analysis, as filtered using SAMtools version 1.9 (37). Duplicated reads, and reads mapping to mitochondria, unassembled contigs, and the ENCODE Blacklist regions were removed using SAMtools. Visualization tracks for each library were generated using deepTools version 2.5.7 (38) function bamCoverage with bin size of 50 bp and normalized using reads per kilobase of transcript per million mapped reads (RPKM). Using RPKM normalized tracks, IgG was subtracted from the corresponding antibody tracks using deepTools function bigwigCompare. To generate read coverage in fixed windows, the genome was binned into 10- or 1-kb bins, and the normalized read count was computed for each bin using deepTools function multiBigwigSummary. Averages of replicates were converted to z scores to account for small differences in dynamic range between experiments. z scores were then smoothed using the mean of rolling, centered windows of size 10 to produce final scores in 10-kb bins. Adjacent bins were merged using bedtools v2.29.2 merge (maximum distance between features, 0) to assign individual domains for further analyses (39). Last, the 10-kb normalized read count was used to generate PCA plots in R version 3.3.1 using the prcomp function from the base packages.

Statistical test for enrichment
Statistical analyses for enrichment were performed using Genomic Association Tester (GAT) (40). The significance of overlap between sets of genomic intervals was calculated on the basis of simulation using a permutation-based approach and accounting for genome organization regions of low mappability. All enrichment analyses were subjected to 1000 simulations. The fold enrichment is expressed as the ratio of observed/expected. P values reflect an estimate of the probability to obtain an observed (or larger) overlap between two segment sets by chance.

Publicly available datasets used in this study
For analysis of genome features and gene expression in murine rod cells, peak coordinates and underlying signal values (when available) for the following datasets were downloaded from Gene Expression Omnibus (GEO) (www.ncbi.nlm.nih.gov/geo/): rod cells: GSE72550 [Assay for Transposase-Accessible Chromatin using sequencing (ATAC-seq): GSM1865011; and RNA: GSM1864999]; and mESCs RNA: GSE89211. Gene annotations were downloaded from University of California Santa Cruz (UCSC) Genome Browser (NCBI38/mm10) Assembly. Gene annotations: GENCODE VM23 release—protein-coding genes only as downloaded from UCSC. For genome feature analyses (fig. S3E), LINEs, SINEs, enhancers (replicated set), and promoters (EPDnew replicated set) were downloaded from UCSC Genome Browser (GRCm38/mm10) (41).

Software and algorithms
Leica Application Suite X (Leica, RRID:SCR_013673), Huygens Software (Scientific Volume Imaging, RRID:SCR_014237), Imaris 9.0.1 (Bitplane, RRID:SCR_007370), GraphPad Prism 9 (GraphPad software, RRID:SCR_002798), SAMtools v1.9 (RRID:SCR_006525) (37), deepTools v2.5.7 (RRID:SCR_016366) (38), R v3.3.1 (R Core Team) (2017, RRID:SCR_001905), bedtools (RRID:SCR_006646) (39), Bowtie2 v2.2.5 (RRID:SCR_016368) (36), and GAT (RRID:SCR_020949) (40).

REFERENCES AND NOTES
1. B. D. Towbin, A. Gonzalez-Sandoval, S. M. Gasser, Mechanisms of heterochromatin subnuclear localization. *Trends Biochem. Sci.* **38**, 356–363 (2013).
2. M. Kohwi, J. R. Lupton, S. L. Lai, M. R. Miller, C. Q. Doe, Developmentally regulated subnuclear genome reorganization restricts neural progenitor competence in Drosophila. *Cell* **152**, 97–108 (2013).

3. R. Stadhouders, G. J. Filion, T. Graf, Transcription factors and 3D genome conformation in cell-fate decisions. *Nature* **569**, 345–354 (2019).

4. M. Amendola, B. van Steensel, Mechanisms and dynamics of nuclear lamina-genome interactions. *Curr. Opin. Cell Biol.* **28**, 61–68 (2014).

5. G. Andrey, S. Mundlos, The three-dimensional genome: Regulating gene expression during pluripotency and development. *Development* **144**, 3646–3658 (2017).

6. W. A. Bickmore, The spatial organization of the human genome. *Annu. Rev. Genomics Hum. Genet.* **14**, 67–84 (2013).

7. A. Buchwalter, J. M. Kaneshiro, M. W. Hetzer, Coaching from the sidelines: The nuclear periphery in genome regulation. *Nat. Rev. Genet.* **20**, 39–50 (2019).

8. I. Solovei, M. Kreysing, C. Lanctôt, S. Kösem, L. Peichl, T. Cremer, J. Guck, B. Joffe, Nuclear architecture of rod photoreceptor cells adapts to vision in mammalian evolution. *Cell* **137**, 356–368 (2009).

9. M. Bustin, T. Misteli, Nongenetic functions of the genome. *Science* **352**, aad6933 (2016).

10. I. Solovei, A. S. Wang, K. Thanisch, C. S. Schmidt, S. Krebs, M. Zwerger, T. V. Cohen, D. Devys, R. Foisner, L. Peichl, H. Herrmann, H. Blum, D. Engelkamp, C. L. Stewart, H. Leonhardt, B. Joffe, LBR and lamin A/C sequentially tether peripheral heterochromatin and inversely regulate differentiation. *Cell* **152**, 584–598 (2013).

11. C. Cepko, Intrinsically different retinal progenitor cells produce specific types of progeny. *Nat. Rev. Neurosci.* **15**, 615–627 (2014).

12. C. L. Cepko, The determination of rod and cone photoreceptor fate. *Annu. Rev. Vis. Sci.* **1**, 211–234 (2015).

13. A. E. Hughes, J. M. Enright, C. A. Myers, S. Q. Shen, J. C. Corbo, Cell type-specific epigenomic analysis reveals a uniquely closed chromatin architecture in mouse rod photoreceptors. *Sci. Rep.* **7**, 43184 (2017).

14. M. Falk, Y. Feodorova, N. Naumova, M. Imakaev, B. R. Lajoie, H. Leonhardt, B. Joffe, J. Dekker, G. Fudenberg, I. Solovei, L. A. Mirny, Heterochromatin drives compartmentalization of inverted and conventional nuclei. *Nature* **570**, 395–399 (2019).

15. P. Mattar, M. Stevanovic, I. Nad, M. Cayouette, Casz1 controls higher-order nuclear organization in rod photoreceptors. *Proc. Natl. Acad. Sci. U.S.A.* **115**, E7987–E7996 (2018).

16. E. Y. Popova, S. A. Grigoryev, Y. Fan, A. I. Skoultchi, S. S. Zhang, C. J. Barnstable, Developmentally regulated linker histone H1c promotes heterochromatin condensation and mediates structural integrity of rod photoreceptors in mouse retina. *J. Biol. Chem.* **288**, 17895–17907 (2013).

17. A. Poleshko, K. M. Mansfield, C. C. Burlingame, M. D. Andrake, N. R. Shah, R. A. Katz, The human protein PRR14 tethers heterochromatin to the nuclear lamina during interphase and mitotic exit. *Cell Rep.* **5**, 292–301 (2013).

18. A. Poleshko, P. P. Shah, M. Gupta, A. Babu, M. P. Morley, L. J. Manderfield, J. L. Ifkovits, D. Calderon, H. Aghajanian, J. E. Sierra-Pagán, Z. Sun, Q. Wang, L. Li, N. C. Dubois, E. E. Morrisey, M. A. Lazar, C. L. Smith, J. A. Epstein, R. Jain, Genome-nuclear lamina interactions regulate cardiac stem cell lineage restriction. *Cell* **171**, 573–587.e14 (2017).

19. C. L. Smith, A. Poleshko, J. A. Epstein, The nuclear periphery is a scaffold for tissue-specific enhancers. *Nucleic Acids Res.* **49**, 6181–6195 (2021).

20. A. Poleshko, C. L. Smith, S. C. Nguyen, P. Sivaramakrishnan, K. G. Wong, J. I. Murray, M. Lakadamyali, E. F. Joyce, R. Jain, J. A. Epstein, H3K9me2 orchestrates inheritance of spatial positioning of peripheral heterochromatin through mitosis. *eLife* **8**, e49278 (2019).

21. W. Meuleman, D. Peric-Hupkes, J. Kind, J. B. Beaudry, L. Pagie, M. Kellis, M. Reinders, L. Wessels, B. van Steensel, Constitutive nuclear lamina-genome interactions are highly conserved and associated with A/T-rich sequence. *Genome Res.* **23**, 270–280 (2013).

22. P. J. Skene, S. Henikoff, An efficient targeted nuclease strategy for high-resolution mapping of DNA binding sites. *eLife* **6**, e21856 (2017).

23. P. P. Shah, W. Lv, J. H. Rhoades, A. Poleshko, D. Abbey, M. A. Caporizzo, R. Linares-Saldana, J. G. Heffler, N. Sayed, D. Thomas, Q. Wang, L. J. Stanton, K. Bedi, M. P. Morley, T. P. Cappola, A. T. Owens, K. B. Margulies, D. B. Frank, J. C. Wu, D. J. Rader, W. Yang, B. L. Prosser, K. Musunuru, R. Jain, Pathogenic LMNA variants disrupt cardiac lamina-chromatin interactions and de-repress alternative fate genes. *Cell Stem Cell* **28**, 938–954.e9 (2021).

24. K. See, Y. Lan, J. Rhoades, R. Jain, C. L. Smith, J. A. Epstein, Lineage-specific reorganization of nuclear peripheral heterochromatin and H3K9me2 domains. *Development* **146**, dev174078 (2019).

25. A. H. Peters, J. E. Mermoud, D. O'Carroll, M. Pagani, D. Schweizer, N. Brockdorff, T. Jenuwein, Histone H3 lysine 9 methylation is an epigenetic imprint of facultative heterochromatin. *Nat. Genet.* **30**, 77–80 (2002).

26. A. Barski, S. Cuddapah, K. Cui, T. Y. Roh, D. E. Schones, Z. Wang, G. Wei, I. Chepelev, K. Zhao, High-resolution profiling of histone methylations in the human genome. *Cell* **129**, 823–837 (2007).

27. K. See, A. A. Kiseleva, C. L. Smith, F. Liu, J. Li, A. Poleshko, J. A. Epstein, Histone methyltransferase activity programs nuclear peripheral genome positioning. *Dev. Biol.* **466**, 90–98 (2020).

28. F. Wang, J. M. Higgins, Histone modifications and mitosis: Countermarks, landmarks, and bookmarks. *Trends Cell Biol.* **23**, 175–184 (2013).

29. J. C. Harr, T. R. Luperchio, X. Wong, E. Cohen, S. J. Wheelan, K. L. Reddy, Directed targeting of chromatin to the nuclear lamina is mediated by chromatin state and A-type lamins. *J. Cell Biol.* **208**, 33–52 (2015).

30. H. Zhao, E. G. Sifakis, N. Sumida, L. Millán-Ariño, B. A. Scholz, J. P. Svensson, X. Chen, A. L. Ronnegren, C. D. Mallet de Lima, F. S. Varnoosfaderani, C. Shi, O. Loseva, S. Yammine, M. Israelsson, L. S. Rathje, B. Németi, E. Fredlund, T. Helleday, M. P. Imreh, A. Göndör, PARP1- and CTCF-mediated interactions between active and repressed chromatin at the lamina promote oscillating transcription. *Mol. Cell* **59**, 984–997 (2015).

31. J. Ahringer, S. M. Gasser, Repressive chromatin in *Caenorhabditis elegans*: Establishment, composition, and function. *Genetics* **208**, 491–511 (2018).

32. D. N. Weinberg, S. Papillon-Cavanagh, H. Chen, Y. Yue, X. Chen, K. N. Rajagopalan, C. Horth, J. T. McGuire, X. Xu, H. Nikbakht, A. E. Lemiesz, D. M. Marchione, M. R. Marunde, M. J. Meiners, M. A. Cheek, M. C. Keogh, E. Bareke, A. Djedid, A. S. Harutyunyan, N. Jabado, B. A. Garcia, H. Li, C. D. Allis, J. Majewski, C. Lu, The histone mark H3K36me2 recruits DNMT3A and shapes the intergenic DNA methylation landscape. *Nature* **573**, 281–286 (2019).

33. S. H. Ahanger, R. N. Delgado, E. Gil, M. A. Cole, J. Zhao, S. J. Hong, A. R. Kriegstein, T. J. Nowakowski, A. A. Pollen, D. A. Lim, Distinct nuclear compartment-associated genome architecture in the developing mammalian brain. *Nat. Neurosci.* 10.1038/s41593-021-00879-5 (2021).

34. Y. Feodorova, M. Koch, S. Bultman, S. Michalakis, I. Solovei, Quick and reliable method for retina dissociation and separation of rod photoreceptor perikarya from adult mice. *MethodsX* **2**, 39–46 (2015).

35. P. J. Skene, J. G. Henikoff, S. Henikoff, Targeted in situ genome-wide profiling with high efficiency for low cell numbers. *Nat. Protoc.* **13**, 1006–1019 (2018).

36. B. Langmead, S. L. Salzberg, Fast gapped-read alignment with Bowtie 2. *Nat. Methods* **9**, 357–359 (2012).

37. G. Badis, M. F. Berger, A. A. Philippakis, S. Talukder, A. R. Gehrke, S. A. Jaeger, E. T. Chan, G. Metzler, A. Vedenko, X. Chen, H. Kuznetsov, C. F. Wang, D. Coburn, D. E. Newburger, Q. Morris, T. R. Hughes, M. L. Bulyk, Diversity and complexity in DNA recognition by transcription factors. *Science* **324**, 1720–1723 (2009).

38. A. E. Bandrowski, J. Cachat, Y. Li, H. M. Müller, P. W. Sternberg, P. Ciccarese, T. Clark, L. Marenco, R. Wang, V. Astakhov, J. S. Grethe, M. E. Martone, A hybrid human and machine resource curation pipeline for the Neuroscience Information Framework. *Database* **2012**, bas005 (2012).

39. A. R. Quinlan, BEDTools: The swiss-army tool for genome feature analysis. *Curr. Protoc. Bioinformatics* **47**, 11.12.1–11.12.34 (2014).

40. A. Heger, C. Webber, M. Goodson, C. P. Ponting, G. Lunter, GAT: A simulation framework for testing the association of genomic intervals. *Bioinformatics* **29**, 2046–2048 (2013).

41. D. U. Gorkin, I. Barozzi, Y. Zhao, Y. Zhang, H. Huang, A. Y. Lee, B. Li, J. Chiou, A. Wildberg, B. Ding, B. Zhang, M. Wang, J. S. Strattan, J. M. Davidson, Y. Qiu, V. Afzal, J. A. Akiyama, I. Plajzer-Frick, C. S. Novak, M. Kato, T. H. Garvin, Q. T. Pham, A. N. Harrington, B. J. Mannion, E. A. Lee, Y. Fukuda-Yuzawa, Y. He, S. Preissl, S. Chee, J. Y. Han, B. A. Williams, D. Trout, H. Amrhein, H. Yang, J. M. Cherry, W. Wang, K. Gaulton, J. R. Ecker, Y. Shen, D. E. Dickel, A. Visel, L. A. Pennacchio, B. Ren, An atlas of dynamic chromatin landscapes in mouse fetal development. *Nature* **583**, 744–750 (2020).

42. A. Mo, C. Luo, F. P. Davis, E. A. Mukamel, G. L. Henry, J. R. Nery, M. A. Urich, S. Picard, R. Lister, S. R. Eddy, M. A. Beer, J. R. Ecker, J. Nathans, Epigenomic landscapes of retinal rods and cones. *eLife* **5**, e11613 (2016).

Citation: C. L. Smith, Y. Lan, R. Jain, J. A. Epstein, A. Poleshko, Global chromatin relabeling accompanies spatial inversion of chromatin in rod photoreceptors. *Sci. Adv.* **7**, eabj3035 (2021).